Investigation of the robustness of time reversal acoustics in solid media through the reconstruction of temporally symmetric sources

2008 J. Phys. D: Appl. Phys. 41 085415

(http://iopscience.iop.org/0022-3727/41/8/085415)

IOP PUBLISHING JOURNAL OF PHYSICS D: APPLIED PHYSICS

J. Phys. D: Appl. Phys. **41** (2008) 085415 (14pp) doi:10.1088/0022-3727/41/8/085415

Investigation of the robustness of time reversal acoustics in solid media through the reconstruction of temporally symmetric sources

M Griffa[1], B E Anderson[1], R A Guyer[1,2], T J Ulrich[1] and P A Johnson[1]

[1] EES-11 (Geophysics), MS D443, Los Alamos National Laboratory, Los Alamos, NM 87545, USA
[2] Department of Physics, University of Massachusetts, Amherst, MA 01003, USA

E-mail: mgriffa@lanl.gov

Received 4 October 2007, in final form 6 February 2008
Published 20 March 2008
Online at stacks.iop.org/JPhysD/41/085415

Abstract
We investigate some of the limitations of time reversal acoustics (TRA) in solid media with transducers attached to the surface. In particular, we consider the limitations due to the finite size of the transducers and elastic wave propagation. Using a theoretical approach, numerical simulations and validation from laboratory ultrasound experiments, we find that finite size transducers and the existence of longitudinal and shear waves play significant roles in perturbing the time reversal process. Despite these limitations, we show that TRA in solids is very robust, providing the means to reconstruct the main features of the source signal. The analysis of TRA retro-focusing properties in solid specimens is of foremost importance for the development of new non-destructive evaluation techniques.

M Movie versions of figures 8, 9, and 10 are available in the online edition at http://stacks.iop.org/JPhysD/41/085415

1. Introduction

Time reversal acoustics (TRA) techniques have been shown to be efficient and robust in focusing acoustic/elastic waves on targets inside a medium [1, 2]. A typical TRA experiment employs an array of transducers (usually called the time reversal mirror, TRM [3, 4]) which can function both as receivers and as transmitters. TRA consists of two propagation stages. In the first stage, called forward propagation, a medium containing scatterers is illuminated by one or more transducers and the TRM records the corresponding elastic wave fields. The source in this first stage can be either the TRM itself (reflection mode), which in turn receives the backscattered waves, or other transducers (transmitting mode), as well as natural sources in the specimen (e.g. acoustic emission sources). The second stage (called time reversal (TR) backpropagation [5, 6]) consists of time reversing the signals and re-broadcasting them into the medium [5, 6].

During the second stage, the wave fields propagate in the reverse direction along the same paths traversed during the forward propagation. They retro-focus on the position(s) of the source(s) and/or point-like scatterers[3]. The retro-focusing takes place automatically since all the information about the positions of the sources/scatterers is encoded in the signals themselves as recovered and recorded during the first stage. This description of the process (called the time reversal process, TRP) is valid when the propagation medium is linear and non-attenuative, the spatial reciprocity principle holds and the medium properties are invariant in time. In fact, the elastodynamic wave equation for a linear, lossless and reciprocal solid medium, whose physical properties do not change in time, is invariant for the time inversion transformation.

Although in the case of attenuative media the symmetry property of the wave equation is no longer valid, the TRP still holds but with decreased efficiency. A detailed explanation of why this happens is contained in appendix A.

Aside from attenuation, the finite size of the transducers constituting the TRM and its finite aperture suggest the TRP is not optimal. Ideally, in the absence of attenuation and in

[3] The retro-focusing occurs also on extended scatterers as long as they can be described as a collection of independent point-like scatterers.

the presence of a closed surface, covered by transducers and surrounding the source location (called time reversal cavity, TRC [6]), the TR retro-focusing process would be nearly perfect (affected only by the absence of the time-reversed version of the evanescent waves locally produced by the source during the forward propagation). However, Cassereau and Fink have shown theoretically that plane 2D TRMs are efficient alternatives to TRCs [7]. Many experimental studies have demonstrated their robustness with this configuration using 1D arrays. However the finite size of the transducers introduces spurious effects due to their electro-mechanical impulse response functions [2–4, 8, 9].

Most of the fundamental parametric studies on the properties of TRA retro-focusing have been conducted in fluids (acoustic wave propagation), including in the ocean [10]. Investigations in solids include TR retro-focusing with only one TRM transducer, using a silicon wafer specimen [11–14] and in full 3D reverberant solids (glass block and fine-grained Berea sandstone) [15]. Additionally, some application-oriented studies have been performed for developing new techniques aimed at the localization of primary or secondary sources (scatterers) in solid specimens [16, 17] using TRMs.

The analysis of TRA retro-focusing properties in solid specimens is very important for the development of new non-destructive evaluation (NDE) techniques. In particular, the combination of the self-adaptive TR retro-focusing properties with nonlinear ultrasonic techniques has led to the development of a suite of techniques for locating and diagnosing cracks and other mechanical damage in solids. This class of techniques relies on Fourier analysis and is termed time reversal nonlinear elastic wave spectroscopy (TR-NEWS). An example is TREND (time reversal elastic nonlinear diagnostics) that is applied to analyse and characterize complex surficial cracks in a bounded solid specimen [18]. TREND exploits the TRP through the automatic focusing of two narrow-band elastic waves, with different central frequencies, onto a scatterer (a crack) on the surface of the specimen. The nonlinearity creates new frequency content from the two basic input frequencies. Thus in TREND the frequency spectrum of the focused signal is analysed for linear combinations of the two basic frequencies and their harmonics [19–21]. Another TR-NEWS technique that exploits the TRP and nonlinear wave mixing for the selective location of nonlinear scatterers, such as micro-cracks, employs the retro-focusing of only the nonlinear components [22–24].

The main goal in developing focusing and imaging techniques based on TRA is to overcome many of the limitations that affect current laboratory ultrasound techniques, such as phased-array imaging [25–27] and the synthetic aperture focusing technique (SAFT) [28, 29], but not the TRP. Potential applications include structural health monitoring of components of aircraft, spacecraft or infrastructure [30, 31], biomedical diagnostic imaging [32, 33] and for medical therapeutic purposes [32, 34–36].

Among the limitations of phased arrays and SAFT are the presence of velocity and mass density heterogeneity inside the propagation medium and at the boundaries. These are sources of diffraction and aberration of wave fronts for most common techniques. Both phased-array imaging techniques and SAFT rely on the ray acoustics description of the propagation process through the specimen to be imaged. Algorithms have been developed in order to extend the range of these techniques to the case of anisotropic homogeneous [37], and anisotropic highly heterogeneous specimens with complicated geometries (see, for example, the inhomogeneous anisotropic SAFT method, InASAFT [38–40]); however, their efficiency in focusing elastic energy onto scatterers dramatically decreases whenever the ray acoustics description is invalid. This is due to, for example, the presence of significant multiple scattering inside the specimen or a wave guide propagation mode [40].

In contrast, TRA can retro-focus elastic energy in the presence of scattering due to inhomogeneities or boundaries [41–44]. It has been shown that TRA takes advantage of multiple scattering in increasing the effective spatial resolution [41]. These properties have been demonstrated in a bounded water channel configuration [42, 45], in shallow water waveguides with complex ocean environments (fluctuating sound speed profiles and varying bottom surfaces) [46–50], in configurations with a random multiply scattering material interposed between the TRM and the region of focusing/imaging [41], and in a thin plate (Lamb wave propagation mode [51]). In the special case of a bounded medium with a geometry resulting in chaotic/ergodic wave front path dynamics, the focusing resolution can be augmented beyond the limits imposed by diffraction [14], using a special TRM configuration integrating an acoustic sink [6, 14].

Another limitation of traditional methods is connected with the frequency-domain response of transducers. They act as filters, increasing the time duration of the received signals at their resonance frequencies. For example, the focal spot on a scatterer location by the InASAFT technique depends upon the pulse-width at the transducer location: wider pulses artificially increase the image spot size [40].

Finally, in phased-array imaging, the number of transducers needed is usually large [27, 52]. Equivalently, the SAFT/InASAFT technique requires a large number of locations on the surface area where the pulse-echo signals are recovered (A-scans). As shown in [40], the larger the number of A-scans, the better the resolution in locating the defects acting like scatterers. This feature increases the complexity of the procedure and apparatus for both the techniques and limits their applications for industrial purposes. In contrast, TRMs are very efficient with a reduced number of elements (relative to phased arrays or SAFT/InASAFT setups) in the presence of reflecting boundaries, such as closed cavities with special geometries or waveguides [11–13, 42]. In addition, TRA techniques automatically account for individual transducer response heterogeneity such as phase mismatching.

The retro-focusing properties of TRA in fluids or with solid specimens submerged in water (with the transducers also submerged) are less complicated than when interrogating solid specimens which have the TRM transducers directly attached to the surface. In fact, because of the fluid environment, in the case of submerged specimens only longitudinal waves propagate and reach the transducers. The configuration with transducers directly attached to the specimens is most

commonly used in NDE and solid materials characterization, in part because submersion is not always practical for such purposes.

The configuration with directly attached transducers is restrictive for the application of a typical TRA experiment. Practically speaking, specimens to be inspected commonly have complicated geometries and the number of transducers used is normally limited. In water tanks, without the limits due to finite size of specimens, the typical number of TRM elements is on the order of one hundred, while, in the case of experimental setups for NDE or materials characterization, usually less than ten and often only one or two TRM transducers are employed.

This limitation might imply a significant reduction of the effective aperture of the TRM and, as a consequence, of the spatial resolution of the retro-focusing process. However, it can be overcome by recording the forward signals at the TRM for a longer time, such that multiple reflections reach the TRM. It has been shown theoretically and experimentally that, in the presence of multiple scattering or multiple reflections, the signal-to-noise ratio of the retro-focus signal in time increases with the length of the TR window (the recording interval at the TRM) until an asymptotic value is reached [53, 13]. The multiple scattering/reflection improves the effective virtual aperture of the TRM, as described by Roux *et al* [42] and Tanter *et al* [54] using the principle of virtual mirrored sources. In closed cavities with a geometry leading to chaotic/ergodic ray paths dynamics, one TR transducer can be sufficient for a near perfect reconstruction of the source, if the TR window is long enough. In bounded media without such geometric properties, the TR window must be longer in order to obtain sufficient mixing of waves and provide enough sampling of the cavity space [12, 13].

The finite size of TRM transducers also causes a loss of spatial information about the forward propagating waves, especially when the size is greater than or equal to the central wavelength applied. In fact, transducers recover the mean value of the wave fields impinging on their surfaces. This response gives rise to the directional nature of a finite-size transducer. Instead of piezo-electric transducers, laser vibrometers can be used for detecting the forward waves. However, the input signals for the TR backward propagation must be re-broadcast into the specimen by means of transducers[4]. This fact creates distortion and blurring in the final TR image.

Complicating aspects of employing TRA in solids includes the presence of longitudinal and shear waves, mode conversion at the boundaries and interfaces and the selective response of piezo-electric transducers to only certain components of the wave fields. Even in a solid specimen submerged in fluid, the solid–fluid interface leads to the generation of two longitudinal waves, one created by the refraction of the longitudinal wave, the other generated by the refraction of the shear-vertical wave within the solid. The shear-horizontal component is totally internally reflected and does not reach the TRM [57]. The information loss due to mode conversion is present (and even more complicated) in the case of a TRA experiment with the transducers attached to the surface of the solid specimen, due to the solid–solid interface at the transducer's face. In addition, single-mode (compressional or shear) transducers, mainly excited by only one vector component of the propagating vector wave field, can only re-broadcast a portion of the total incident field.

The purpose of this work is to present the results of a set of studies, both theoretical and experimental, aimed at investigating the robustness and efficiency of TRA in solids using TRMs bonded directly to their surfaces. These issues were first addressed by Delsanto *et al* [58] with numerical simulations and by Sutin *et al* [15] experimentally. We show that the finite size of TRM transducers and the small number of TR elements used do not significantly degrade the retro-focusing.

In section 2 we present the general approach, followed, in section 3, by a theoretical investigation of a *gedanken* (thought) TRA experiment in elastic media, with embedded point-like source and receiver. Appendix B shows some general properties of convolution integrals used in the theoretical analysis while appendix C completes it with the extension of the formulation to the case of an extended source and receiver. Section 4 describes the validation of the theoretical treatment using numerical simulations in 2D and section 5 reports the results of laboratory experiments.

2. General approach

A criterion for evaluating the robustness of TRA experiments is the analysis of the quality of the reconstruction of band-limited temporally symmetric source signals. We consider the following TRA experiment both numerically and experimentally: TR reconstruction of a temporally symmetric source signal injected into the specimen by a single, finite-size transducer bonded to the surface of the specimen acting as a transmitter during the forward propagation and as a receiver during the backpropagation. We consider a solid specimen with parallelepiped geometry. The same type of a TRA experiment is performed twice. In one case the diameter of the TRM transducer is larger than the central wavelength of the propagating wave packet, while in the other it is smaller. We choose these two types of experiments in order to investigate the role of the finite size of transducers in the TR source reconstruction process and to make broader inferences.

We intentionally select a configuration that does not favour the TR process. The geometry of the specimen does lead to multiple reflections at its boundaries but the wave front path dynamics are not ergodic. A long TR window is chosen in order to guarantee sufficient mixing of the wave front paths for achieving retro-focusing with only one TRM transducer. Its finite size implies the loss of a significant amount of information regarding the forward propagation. Finally, as previously mentioned, we consider a TRM transducer operating only in compressional mode, i.e. it can be excited only by the components of the different vector wave fields

[4] Some thermoelastic techniques, involving high power laser pulses incident on the surface of the specimen, have been used in TRA experiments [55, 56], especially for the generation of surface sound/ultrasound waves, but they are not feasible for all types of TRA experiments with solid media.

impinging on its surface along the orthogonal direction[5]. The above characteristics are selected because they are typical for NDE inspection of solid specimens, as well as numerous laboratory experiments.

3. Theoretical analysis

As a starting point, we consider an elastic medium under the following three general hypotheses, (I) the elastic wave propagation through the medium is completely linear, (II) spatial reciprocity is valid throughout the whole medium, (III) the elastic wave propagation properties of the medium are considered stationary in time, i.e. the Green function of the medium for any pair of points is invariant under time shift transformations.

We consider two ideal point-like transducers, A and B, located in the medium at different positions $\boldsymbol{r}_A$ and $\boldsymbol{r}_B$. A is the source of the forward propagation and B the only TRM transducer. At time $t = 0$ the source at A emits a signal (a pulse, for example) symmetric about $t = 0$, $s(t)$. The resultant signal at B, $s_B(t)$, is recorded during the time interval $[0; t_R]$. The corresponding time-reversed version of this signal, $s_B^-(t) = s_B(t_R - t)$, is re-broadcast (assuming that $t = 0$ is the start time of the backward propagation). The induced signal at A, $s_A(t)$, is recorded during the backpropagation in order to compare it with the time-reversed version of the source signal $s(t)$.

The signal $s_A(t)$ is monitored in the time interval $[0; 2t_R]$. The TR reconstruction of the source signal should occur at time $t = t_R$. We want to analyse the temporal symmetry properties of $s_A(t)$ around time $t = t_R$ of the backward propagation.

We consider the Green function $G(\boldsymbol{r}, \boldsymbol{r}', t, t')$ of the elastodynamics wave equation for a specific mode of propagation in an unbounded elastic medium (either longitudinal or shear wave propagation) written for the potentials [59]. G is the solution to the scalar wave equation of the type $((1/c_i^2)(\partial/\partial t) - \Delta)G(\boldsymbol{r}, \boldsymbol{r}', t, t') = \delta(\boldsymbol{r} - \boldsymbol{r}')\delta(t - t')$. c_i is the phase velocity of either the longitudinal or shear wave propagation mode. $\partial/\partial t$ and Δ are, respectively, the first-order partial time derivative operator and the Laplacian operator in 2D space (x, y). The right-hand side term in the equation represents a point-like source in space and in time. Due to the hypothesis of a time invariant medium, $G(\boldsymbol{r}, \boldsymbol{r}', t, t') = G(\boldsymbol{r}, \boldsymbol{r}', t - t', 0)$.

We define $G_{A,B}(t, t') = \tilde{G}_{A,B}(t - t')$ to be the Green function of the medium from point B to point A, with a source at B starting at time $t = t'$, $G_{A,B}(t, t') = G(\boldsymbol{r}_A, \boldsymbol{r}_B, t, t') = G(\boldsymbol{r}_A, \boldsymbol{r}_B, t - t', 0)$.

For example, in the case of a linear non-viscous fluid unbounded medium, $G_{A,B}(t, t') = (1/4\pi\|\boldsymbol{r}_A - \boldsymbol{r}_B\|)\delta(t - t' - \|\boldsymbol{r}_A - \boldsymbol{r}_B\|/c)$, where $\|\cdot\|$ indicates the standard Euclidean vector norm and c is the wave propagation speed in the fluid. In the case of a solid medium, elastically isotropic or anisotropic, homogeneous or inhomogeneous, $\tilde{G}_{A,B}(t - t')$ assumes more complicated forms [60].

$s_A(t)$ can then be calculated using the medium Green function (propagator) [61],

$$s_A(t) = \big(\tilde{G}_{A,B}(t') *_{t'} s_B^-(t')\big)(t) = \int_{-\infty}^{+\infty} \mathrm{d}t' \tilde{G}_{A,B}(t - t') s_B^-(t'), \quad \forall t \in [0; 2t_R], \tag{1}$$

where $(\cdot *_{t'} \cdot)(t)$ indicates the convolution-in-time integral function, evaluated at time t, of two signals, in this case the Green function for the couple of points $(\boldsymbol{r}_A, \boldsymbol{r}_B)$ and the time-reversed signal $s_B^-(t)$.

Equation (1) can be rewritten as

$$s_A(t) = \int_{-\infty}^{+\infty} \mathrm{d}t'' \tilde{G}_{A,B}(t - t'') s_B^-(t'' + t_R) = \int_{-\infty}^{+\infty} \mathrm{d}t'' \tilde{G}_{A,B}(t - t'') s_B(-t''), \tag{2}$$

where the change in time variable $t'' = t' - t_R$ and hypothesis (III) have been applied to equation (1). Note that this change in time frame of reference implies that both the integration variable t'' and the evaluation time t during the backward propagation can assume values in the range $[-t_R; t_R]$. That implies that the argument of the s_B signal can be negative, in the range $[-t_R; 0]$, and the retro-focal time is $t = 0$ in this new temporal frame of reference.

Equation (2) can be rewritten as

$$s_A(t) = \big(\tilde{G}_{A,B}(t') *_{t'} s_B(-t')\big)(t), \qquad \forall t \in [-t_R; t_R]. \tag{3}$$

According to the first property shown in appendix B, equation (B.4), $s_B(-t')$ can be written as

$$s_B(-t') = \int_{-\infty}^{+\infty} \mathrm{d}t'' \tilde{G}_{B,A}(-t' - t'') s(t'') = \big(\tilde{G}_{B,A}(-t'') *_{t''} s(-t'')\big)(t'). \tag{4}$$

Then, equation (3) can be rewritten as

$$s_A(t) = \big(\tilde{G}_{A,B}(t') *_{t'} \tilde{G}_{B,A}(-t') *_{t'} s(-t')\big)(t), \quad \forall t \in [-t_R; t_R]. \tag{5}$$

Considering hypothesis (II) at the beginning of the section (spatial reciprocity principle), equation (5) can be rewritten as

$$s_A(t) = \big[\big(\tilde{G}_{A,B}(t'') *_{t''} \tilde{G}_{A,B}(-t'')\big)(t') *_{t'} s(-t')\big](t), \quad \forall t \in [-t_R; t_R]. \tag{6}$$

In equation (6), the term within the round parentheses corresponds to the definition of the auto-correlation function of the Green function $\tilde{G}_{A,B}(t)$ (see property II in appendix B), which is a symmetric function about $t = 0$ (see property II in appendix B). Property IV in appendix B shows that the convolution-in-time of two even functions gives as a result an even function. Equation (6) defines the signal $s_A(t)$ as the convolution-in-time of two signals symmetric about $t = 0$ (for initial definition, $s(t)$ is an even function), then $s_A(t)$ is symmetric about $t = 0$ too, i.e. it is symmetric about the retro-focal time.

This demonstration is based only on the time domain properties of the Green function of the medium derived from

[5] We could consider also shear-mode transducers, that are sensitive only to shear deformations. However, the basic issue we would like to underline with this work is the fact that transducers commonly used in NDE procedures are usually compressional or shear. In both cases part of the forward wave propagation information is lost.

the three hypotheses stated at the beginning of the section, so that it is generally valid independent of its spatial dependence. It relies essentially on the same hypotheses sufficient to show that the TRP realizes a spatial-temporal matched-filter [2,5,54,62], focusing wave energy with maximum value at the original source location and at the retro-focal time. However, the realization of a spatial-temporal matched filter does not guarantee the perfect realization of the TRP, i.e. the perfect reconstruction in time and space of the forward propagation source field. The demonstration developed here shows that at least the temporal symmetry of the original source signal is conserved by the TRP.

This result, obtained for the case of a point-like source in A and a point-like TRM receiver in B, can be extended to the case of sources and receivers with finite sizes. Indeed, consider a source in a region R_A (a 2D manifold embedded in 3D Euclidean vector space R^3). It emits a temporally symmetric pulse around time $t = 0$. This produces a signal recorded through a receiving region R_B. Then re-broadcasting the TR version of that signal from R_B (now acting as a transmitter) gives rise to a TR focused signal within the region R_A. This last signal is temporally symmetric about $t = 0$, which corresponds to the retro-focal time.

In laboratory experiments, the electrical signal produced by (compressional) transducers, e.g. in receiving mode, results from the mean value of the surficial out-of-plane component of the vector wave field (displacement or velocity) across the transducer surface. For the transmitting mode, the electrical signal induces a wave field in the medium (e.g. diagonal component of the stress tensor field) whose normal partial derivative is proportional to the TR of the received normal component of the corresponding conjugated wave field (e.g. normal component of the velocity vector wave field) [63–67]. As a consequence of the behaviour of real transducers in receiving and transmitting modes, the transmitted wave field from R_A during the forward propagation can be calculated as its mean value on R_A. The same is valid for the received wave field on R_B. Then, under hypothesis (I) (linearity of the medium), equation (6) can be rewritten using integration over the regions R_A and R_B, such that the result is still valid. See appendix C for the details.

4. Validation by numerical simulations

4.1. Setup

Figures 1(*a*) and (*b*) show the geometry and configuration of two numerical simulations, performed in 2D. In both cases, a specimen is selected with rectangular shape and sizes $L_x = 133.21$ mm and $L_y = 88.875$ mm, the same geometry of a 2D (diagonal) slice extracted from a 3D parallelepiped solid used in the laboratory experiments (see section 5.1), intersecting the positions of the actual transducers attached to the 3D specimen (see figure 2 for its schematic representation). Simulations are performed only in 2D in order to obtain a preliminary validation of the robustness of TRA retro-focusing in reconstructing the source signal, at the right spatial location and with the right features (temporal symmetry), in a closed

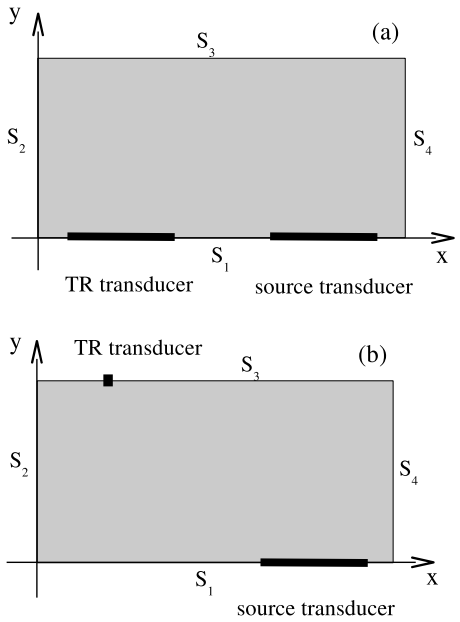

Figure 1. (*a*) Schematic representation of the numerical simulation setup in the case of a relatively large TRM transducer (compared with the central wavelength of the wave fields). (*b*) Same setup for the numerical simulation but for a small TRM transducer, in this case the opposite face with respect to the previous case. Notice that in both cases, the source transducer is positioned on the same side of the specimen and has the same geometrical and physical characteristics (length = 38 mm).

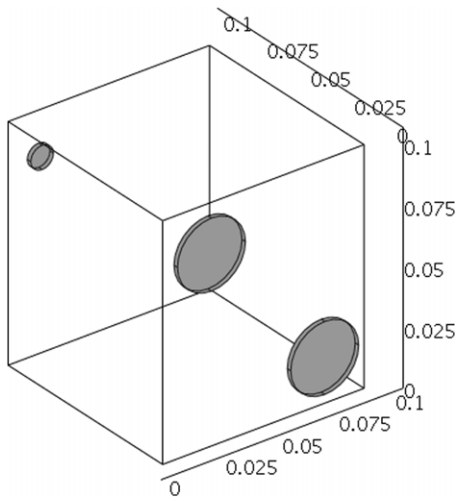

Figure 2. Schematic representation of the specimen (a quasi-cubic glass block) used in the laboratory experiments, with one big source transducer and two TRM transducers, one placed on the same lateral face as the source and identical to it, the other one on the opposite lateral face of the block and with smaller diameter. All the transducers are piezo-ceramic circular disks. The small TRM transducer has diameter = 4 mm.

solid. In a full 3D parallelepiped specimen with reflecting boundaries, the TR reconstruction is expected to be improved due to an increased mixing of the wave fronts' paths (reflections in 3D instead of 2D), as shown by the experimental results in section 5.2. Increasing wave front mixing nearly leads to ergodic/chaotic path dynamics (although not complete, in this case, due to the selected specimen geometry) . This means

an improvement of the retro-focusing properties of a single-transducer TRM, as reported in [13].

The sample is a homogeneous isotropic solid with Lamé's constants $\lambda = 75.1\,\text{GPa}$ and $\mu = 31.2\,\text{GPa}$, volumetric mass density $\rho = 6.79 \times 10^3\,\text{kg m}^{-3}$ and quality factor $Q = 2 \times 10^3$. These parameters are derived from experimental measurements of the longitudinal phase velocity, amplitude attenuation coefficient and mass of the parallelepiped doped glass specimen used in the laboratory experiments (see section 5.1).

The two Cartesian components, $u(\boldsymbol{r}, t)$ (x-axis) and $v(\boldsymbol{r}, t)$ (y-axis), of the displacement vector wave field ($\boldsymbol{u}(\boldsymbol{r}, t)$) are calculated in the plane of the rectangle solving the 2D partial differential equation problem consisting of the elastodynamic wave equation, the boundary conditions and the initial conditions. The 2D elastodynamic wave equation can be written in the vectorial form, in terms of the displacement vector wave field $\boldsymbol{u}(\boldsymbol{r}, t)$:

$$\rho \frac{\partial^2 \boldsymbol{u}}{\partial t^2} = (\lambda + 2\mu) \cdot \vec{\nabla}(\vec{\nabla} \cdot \boldsymbol{u}) - \mu \vec{\nabla} \wedge \vec{\nabla} \wedge \vec{\nabla} \boldsymbol{u}, \qquad (7)$$

where $\cdot$ indicates the standard Cartesian (dot) product between vectors, $\wedge$ the external (cross) one and $\vec{\nabla}$ is the 2D vectorial differential operator with components $(\partial/\partial x, \partial/\partial y)$.

Free boundary conditions are applied, in both simulations, for three of the four sides of the rectangular specimen, S_1, S_2, S_3, which are the sides lying on $y = 0$, $x = 0$, $y = 88.875\,\text{mm}$, respectively. These conditions are expressed as follows:

$$\epsilon_{ij}(\boldsymbol{r}, t) = 0, \qquad \forall i, j = 1, 2, \quad \forall t > 0 \quad \text{and}$$
$$\forall \boldsymbol{r} \in S_1 \cup S_2 \cup S_3, \qquad (8)$$

where $\cup$ indicates the union set operation and $\epsilon_{ij}(\boldsymbol{r}, t)$ are the components of the linear strain tensor wave field under the approximation of small deformations, defined as

$$\begin{cases} \epsilon_{11}(\boldsymbol{r}, t) = \dfrac{\partial u}{\partial x}(\boldsymbol{r}, t), \\ \epsilon_{22}(\boldsymbol{r}, t) = \dfrac{\partial v}{\partial y}(\boldsymbol{r}, t), \\ \epsilon_{12}(\boldsymbol{r}, t) = \dfrac{1}{2}((\partial u/\partial y) + (\partial v/\partial x))(\boldsymbol{r}, t), \\ \epsilon_{12}(\boldsymbol{r}, t) = \epsilon_{21}(\boldsymbol{r}, t), \end{cases} \qquad (9)$$

the last row stating the symmetry property of the strain tensor field.

Fixed boundary conditions are applied in each simulation to the remaining side of the specimen, S_4, along the vertical line $x = 133.21\,\text{mm}$, imposing

$$\boldsymbol{u}(\boldsymbol{r}, t) = \boldsymbol{0}, \qquad \forall t \geqslant 0 \quad \text{and} \quad \forall \boldsymbol{r} \in S_4. \qquad (10)$$

In both simulations, the initial conditions are

$$\boldsymbol{u}(\boldsymbol{r}, t = 0) = \boldsymbol{0}, \qquad \forall \boldsymbol{r}. \qquad (11)$$

An additional boundary condition consists in the simulated source transducer, implemented as a segment of length $L_{\text{TR}} = 38\,\text{mm}$, lying on the $y = 0$ axis (S_1 side of the specimen), with centre in the position (91.0;0.0). In this part of the boundary, within a limited time interval $[0; t_f]$

$$v(x, y = 0, t) = s(x, t)$$
$$= -S \exp\left[-0.5\left(\frac{x - x_0}{\sigma_x}\right)\right] \exp\left[-0.5\left(\frac{t - t^*}{\sigma_t}\right)\right]$$
$$\times \sin(2\pi f \cdot (t - t_0)) \cdot H(t - t_0) \cdot H(t_f - t). \qquad (12)$$

Equation (12) represents the injection into the specimen of the y component of the displacement vector (compressional transducer). The temporal evolution is modelled as 3.5 cycles of a sine wave signal with amplitude modulated by a Gaussian profile and frequency $f = 200\,\text{kHz}$. In equation (12), S represents the maximum value of the amplitude, $t_0 = 0.5\,\mu\text{s}$ is the initial time for the pulse, $t_f = t_0 + (3.5/f) = 18\,\mu\text{s}$ is the final time of injection, $t^* = t_0 + (1.75/f) = 9.25\,\mu\text{s}$ is the centre of the Gaussian envelope for the amplitude of the pulse, $\sigma_t = (0.4/f) = 2\,\mu\text{s}$ is the standard deviation of the Gaussian envelope, $H(t)$ is the Heaviside step function, $x_0 = 91\,\text{mm}$ and $\sigma_x = 8\,\text{mm}$. Figure 3(b) shows the waveform.

In equation (12) there is also a multiplication term of the form of a Gaussian envelope along the spatial x-axis introduced as a modulation term along the extension of the simulated transducer. The function is centred on the centre of the transducer, $x_0 = 91\,\text{mm}$. The spatial modulation for the amplitude of the source signal is introduced in order to simulate the effective active region of the source transducer. Indeed, actual measurements show that the active region does not correspond to the full surface [68, 69] due to the fact that the source transducer is large compared with the central wavelength of the source pulse ($\lambda = 22.5\,\text{mm}$).

The initial-boundary value differential problem defined by equations (7) and (8) and (10)–(12) is solved numerically through a finite difference time domain (FDTD) computational code based on the local interaction simulation approach [70–73], a method specifically designed to the solution of elastodynamics problems using a common theoretical and algorithmic framework independent of the complexity of the material (linear or nonlinear elastic, homogeneous or highly heterogeneous). The discretization step of the mesh is $\Delta\varepsilon = 0.1125\,\text{mm}$, corresponding to about 200 nodes per central wavelength. The time step used is $\tau = 0.02\,\mu\text{s}$. The convergence of the finite difference code is based upon satisfying the Courant–Friedrichs–Lewy [74] criterion. Its stability has been proven elsewhere [75, 76] for similar case studies with a similar high number of spatial lattice nodes per central wavelength.

The displacement vector wave field $\boldsymbol{u}(\boldsymbol{r}, t)$ thus calculated is recorded during the forward propagation stage along the line representing the TRM transducer, now acting as a receiver. In the two different simulations, the TRM receiver is located in different positions (opposite sides of the specimen) and has distinct sizes. Figure 1(a) shows the configuration of the simulation with an extended 1D TRM transducer with length $L_{\text{TR}} = 38\,\text{mm}$, its centre being placed at the point with coordinates (32.0;0.0) mm. Figure 1(b) shows the configuration for the second simulation, identical to the first one except for the TRM transducer, where the length

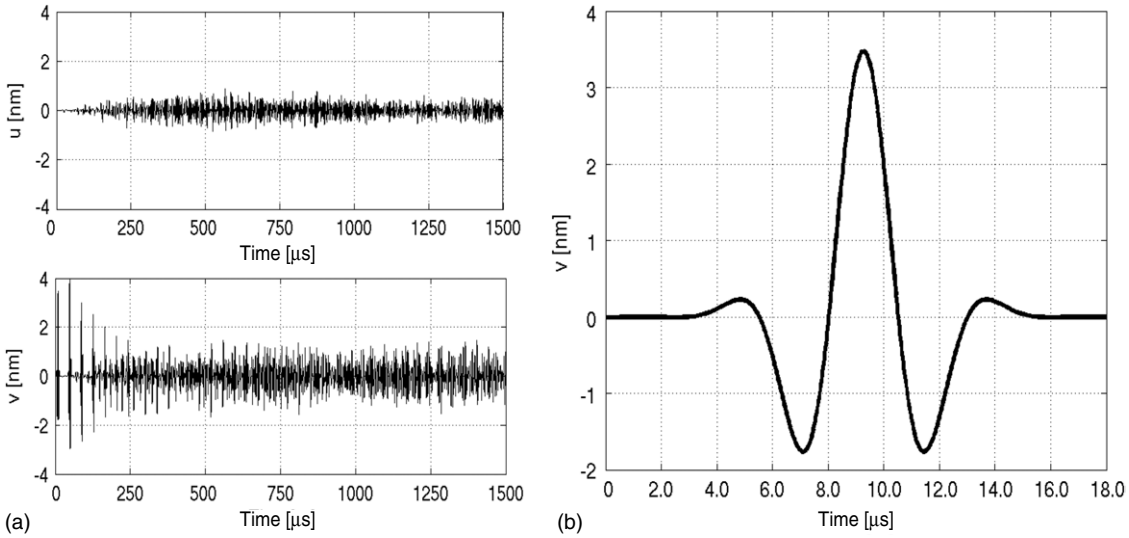

Figure 3. (*a*) Spatial-average along the source transducer length of the horizontal (x) and vertical (y) components of the displacement vector wave field recorded during the simulated forward propagation. Top: horizontal component ($\langle u\rangle_x(t)$). Bottom: vertical component ($\langle v\rangle_x(t)$). (*b*) Time series of the spatial-average of the vertical component ($\langle v\rangle_x(t)$) of the displacement vector wave field across the source extension, ($\langle v\rangle_x(t)$), during the injection, shown in order to visualize the temporally symmetric displacement source signal applied to that part of the specimen boundary.

$L_{\mathrm{TR}} = 4$ mm and the centre is positioned at (32.0;88.875) mm, on the opposite boundary.

A time window (called TR window) is extracted excluding the time onset corresponding to the time of flight from the source line to the receiving line. The portion of the received v wave field in this temporal interval is time reversed, spatially averaged along the extension of the transducer and used as input for the backpropagation. We use this procedure in order to take into account the typical averaging effect occurring during the transducer detection process that generates the electrical signals at the transducers. It is a first-order approximation for modelling a piezo-electric transducer as a baffled planar piston [64–67].

4.2. Results

Figure 3(*a*) shows the spatially averaged horizontal (x) and vertical (y) components of the displacement vector field recorded at the line source during the forward propagation. The two displacement signals are indicated as $\langle u(x, y = 0, t)\rangle_x(t)$ and $\langle v(x, y = 0, t)\rangle_x(t)$, respectively, where $\langle\rangle_x$ indicates spatial averaging along the $x-$axis. Figure 3(*b*) is a close-up of the source waveform. The time length of the forward propagation simulation is approximately $\Delta t_{\mathrm{simul}} = 1500\,\mu$s, long enough for obtaining sufficient sampling of the medium space by the multiple reflected wave fronts. After the injection, the source line becomes passive. The multiple reflections can be seen (see figure 3(*a*)) after about 250 μs: the signal observed at the source location becomes very complicated, due to interference effects among the different reflected signals. As a consequence of non-ergodicity, in both numerical simulations the single element TRM is not able to encode all the information regarding the reverberant wave fronts inside the cavity, as reported in figures 4 and 5, respectively for the two simulations.

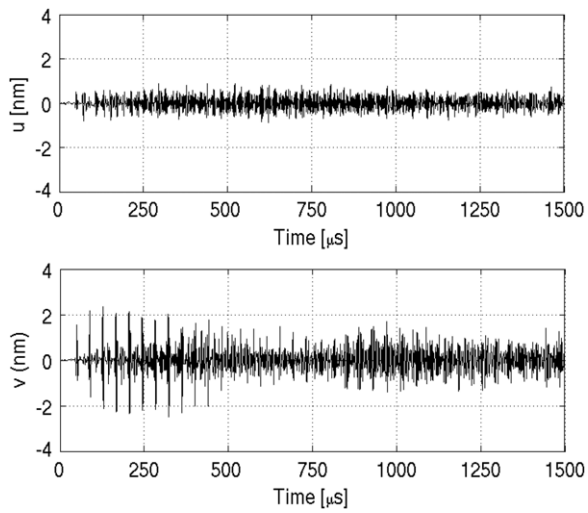

Figure 4. Received signal at the TRM transducer during the forward propagation. Simulation with a large (length = 38 mm) TRM transducer. Top: horizontal (x) component of the displacement vector wave field calculated as its spatial-average along its length ($\langle u\rangle_x(t)$). Bottom: vertical (y) component of the same vector wave field (spatial-average of, $\langle v\rangle_x(t)$).

We note that during and after the source injection, the displacement vector wave field acquires a horizontal (x-) component due to the Poisson effect. This component is not recorded by the compressional-mode transducers. This is another source of information loss. In both simulations, the TRM transducer re-broadcasts only the time-reversed version of the space-average vertical component of the displacement vector wave field.

Figures 6(*a*) and 7(*a*) report the backpropagation results regarding the spatially averaged vertical component of the displacement vector wave field ($\langle v\rangle_x(t)$) across the location of the original source. The temporal axis of both figures is redefined such that $t = 0$ corresponds to the retro-focusing

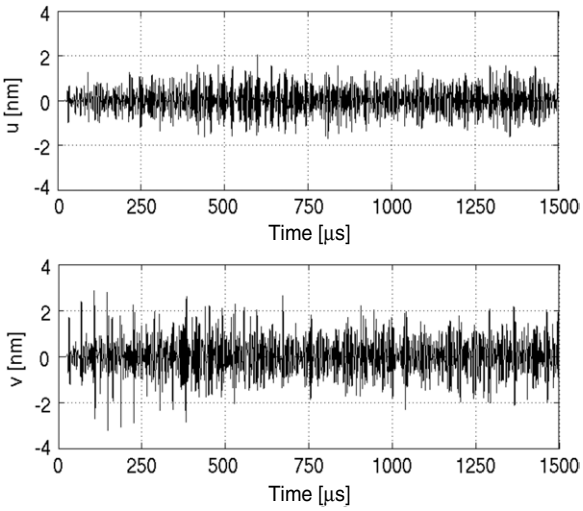

Figure 5. Received signal at the TRM transducer during the forward propagation. Simulation with a small (length = 4 mm) TRM transducer. Top: horizontal (x) component of the displacement vector wave field calculated as its spatial-average along its extension ($\langle u \rangle_x(t)$). Bottom: vertical (y) component of the same vector wave field (spatial-average of, $\langle v \rangle_x(t)$).

time. Meaning, the time at which the maximum peak amplitude of the source signal is recreated.

In both experiments, the TR time window ends at $t = 1499\ \mu$s but it starts at $t = 10\ \mu$s and $t = 24\ \mu$s for the case with the large TR transducer and the case with the small one respectively. This difference is due to the respective positions on the boundaries of the specimen. The full signal, including the coda, i.e. the part due to the multiple reflections inside the specimen, is used for TR in both experiments.

As shown in figures 6(a) and 7(a), a higher amplitude waveform appears at the focal time. Figures 6(b) and 7(b) show that those waveforms are similar to the original source signals and are relatively symmetric around the focal time. In the two cases, different losses of information from the forward propagation occur. With the big TRM transducer, more information about the forward propagating waves is collected but it is lost due to the spatial averaging process. With the small TRM transducer, less space on the boundary is covered, so it collects less information about the incident wave fields.

However, in both cases the received waveform is in good agreement with the source. The TR window length proves to be long enough to achieve the retro-focusing[6]. In both cases, the reconstructed source signal at the source location has a smaller amplitude than the original due to the space-averaging effects of the transducers, to their finite size and to the attenuation within the medium acting like a spatial frequency filter during the propagation [54]. As discussed in section 1, this degrades the retro-focusing process. At about 8.75 μs post retro-focusing time, the TR backward propagation stage of the experiment is complete. In absence of an *acoustic sink* [6, 14], the interference of the incoming backward waves

[6] Additional simulations we run have proved that either increasing the number of TRM channels or the length of the TR window does not lead to a significant change in the retro-focusing quality (results not reported for brevity).

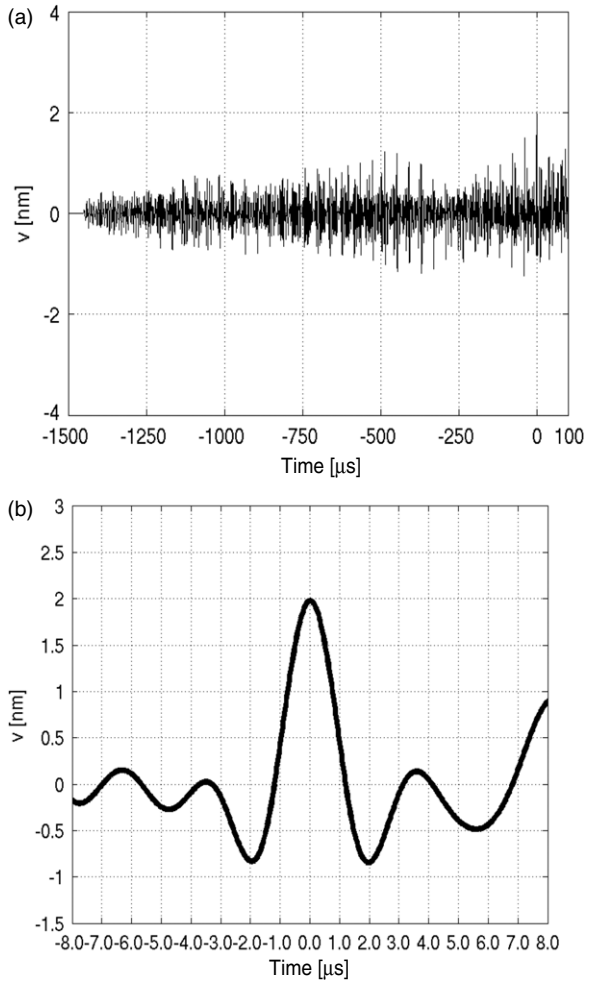

Figure 6. (a) Retro-focused signal at the original source location calculated as the spatial-average of the vertical (y) component of the displacement vector wave field ($\langle v \rangle_x(t)$). The time axis has been shifted in order to have 0 as the retro-focal time. (b) Close-up around the retro-focal time of the same time series. Numerical simulation for the case with the large TRM receiver.

at the original source location gives rise to their outward scattering such that new forward propagation commences. This process is due to diffraction: the energy associated with the incoming backward waves is not re-absorbed at the focus and it is therefore scattered in the form of diverging waves.

Figure 8 shows a grey scale plot of the norm of the displacement vector wave field ($||\boldsymbol{u}(\boldsymbol{r}, t)||$) at time $t = 9.00\ \mu$s, at the time the peak of the source signal is going to be injected into the medium during the forward propagation. Figures 9 and 10 show the same type of plot for the backpropagated wave field, close to the time of retro-focusing for the two cases (large and small TRM transducers, respectively). From figure 9 it is clear that the largest amplitude is localized at the original source, meaning that constructive interference occurs mostly in that region of the specimen. The same result is obtained in the case with the small TRM transducer as shown by figure 10. However, figure 10 shows a clearer focus at the source location, while in the previous case one can see from figure 9 that more

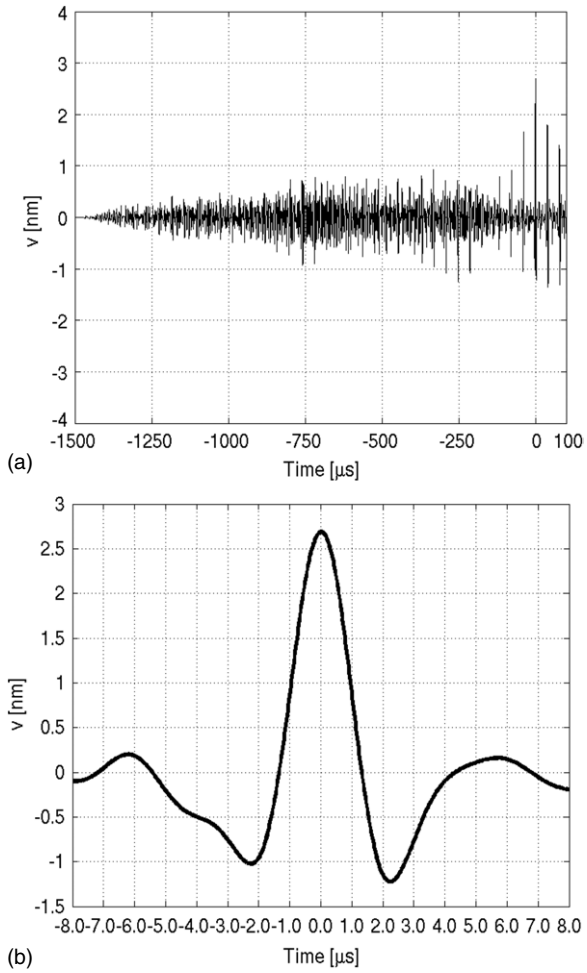

Figure 7. (*a*) Retro-focused signal at the forward propagation source location calculated as the spatial-average of the vertical (y) component of the displacement vector wave field ($\langle v \rangle_x(t)$). The time axis has been shifted in order to have 0 as the retro-focal time. (*b*) Close-up around the retro-focal time of the same time series. Numerical simulation for the case with the small TRM receiver.

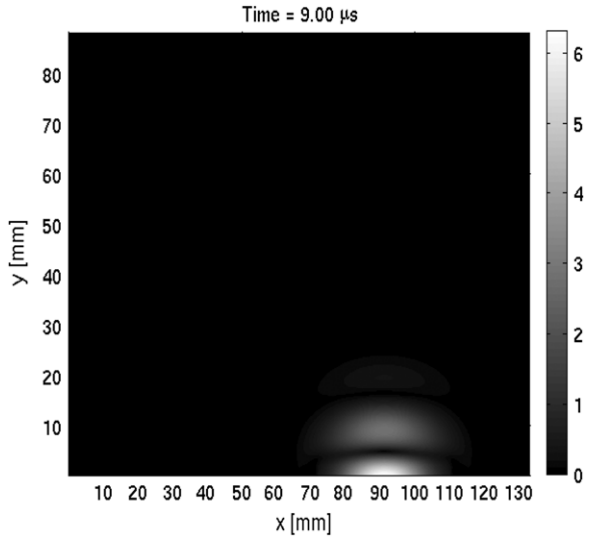

Figure 8. Greyscale plot of the norm of the displacement vector wave field during the simulated forward propagation at time $t = 9\,\mu$s since the beginning, at the time when the peak of the source signal is going to be injected into the medium (it exactly occurs at $t = 9.25\,\mu$s). See additional material for the movie of part of the simulation of the forward propagation. A movie version of this figure is available at http://stacks.iop.org/JPhysD/41/085415.

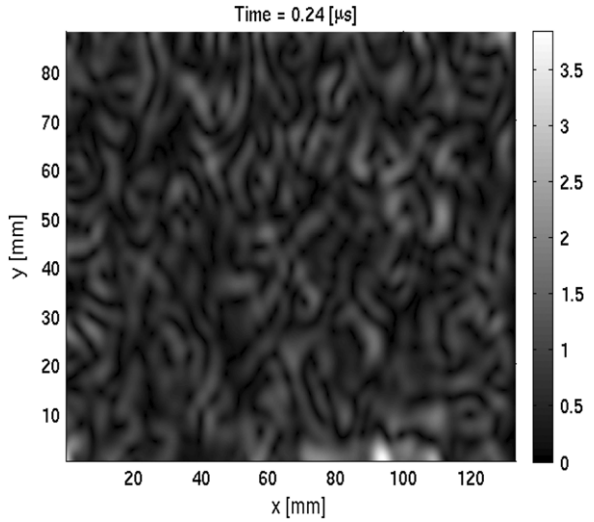

Figure 9. Greyscale plot of the norm of the displacement vector wave field during the simulated TR backpropagation calculated just after the TR focusing time. Case with the large TRM transducer. See additional material for the movie of part of the simulation of the TR backpropagation. A movie version of this figure is available at http://stacks.iop.org/JPhysD/41/085415.

elastic energy is redistributed about the medium. The source directivity plays an important role as well, re-distributing the energy significantly in contrast to the forward propagation. This is an important issue.

5. Validation by laboratory experiments

5.1. Setup

Figure 2 shows a schematic representation of the 3D specimen used in the laboratory experiments along with the approximate locations of the source transducer (near the lower right corner of the frontal face), the large TRM transducer (near the top left corner of the frontal face) and the small TRM transducer (opposite face). The size of the specimen is 88.875 mm × 88.875 mm × 99.2 mm and its total mass is $M = 4.90$ kg. The physical parameters of the specimen modelled in the numerical study derive from measurements on this sample.

In both experiments, a source signal of the same type as that used in the simulations described in section 4.1 (see equation (12)) is considered, 3.5 cycles of a sine wave with central frequency $f = 200$ kHz, amplitude modulated in time by a Gaussian profile and pulse-width in time equal to 16 μs, resulting in a temporally symmetric pulse around $t = 8\,\mu$s ($t_0 = 0\,\mu$s). The transducers used are piezo-ceramic compressional mode, PZT 5 type, with thickness of 2 mm, the large ones with diameter of 38 mm were produced by APC International Ltd., while the small one with diameter of 4 mm was manufactured by Boston Piezo-Optics Inc. The

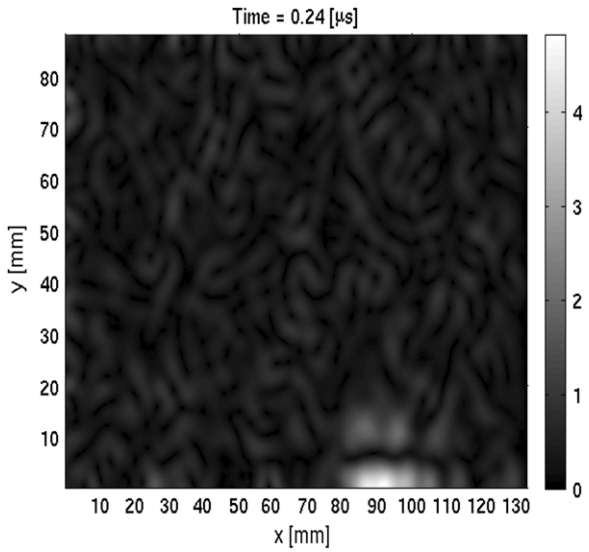

Figure 10. Greyscale plot of the norm of the displacement vector wave field during the simulated TR backpropagation calculated just after the TR focusing time. Case of the small TRM transducer. See additional material for the movie of part of the simulation of the TR backpropagation. A movie version of this figure is available at http://stacks.iop.org/JPhysD/41/085415.

transducers only apply vertical (y-component) displacements to the specimen surface ($v(x, y = 0$ or $y = 88.875\,\text{mm}, t)$). The single channel TRM apparatus used is similar to the one described in figure 3 of [18].

Both TR source reconstruction experiments follow the same procedure described for the simulations. The large source transducer emits the source signal that produces propagating wave fields recorded by the TRM transducer (located in two different positions for the two respective experiments) using a TR window of duration 1640 μs. This time interval excludes the initial interval before the first arrival and guarantees sufficient mixing of wave fronts multiply reflected at the boundaries. That signal is time reversed and re-injected into the specimen and the resultant signal is recorded at the original source transducer.

5.2. Results

Figures 11(a) and 12(a) show the time series for the vertical component of the displacement vector wave field ($\langle v(x, y = 0\,\text{mm}, t)\rangle_x(t)$) at the original source location, for the large and the small TRM transducers, respectively. A high pass filter is applied to the retro-focal signal of the large TRM transducer case, filtering out the frequencies below 120 kHz. In fact, the large TRM transducer has a resonance frequency of about 75 kHz, producing a significant time lengthening of the re-broadcast signal, whereas the small transducer has much higher resonance frequencies. Both figures show that the original waveform of the source is not perfectly reconstructed. However, both TR focused signals have a high degree of symmetry around the focal time, defined to be at $t = 0\,\mu$s. Figures 11(b) and 12(b) present a close-up of the same signal of figures 11(a) and 12(a), respectively, about the focus time.

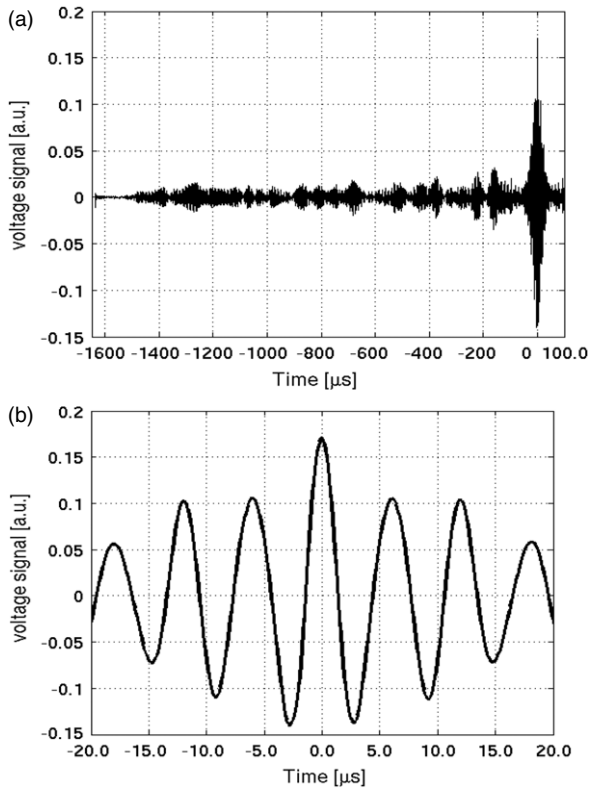

Figure 11. (a) Retro-focal signal at the forward propagation source location. The time axis has been shifted to 0 as the retro-focal time. (b) Close-up around the retro-focal time. Experimental results for the case with the large TRM receiver.

They show a high level of symmetry for a time interval of $\pm 20\,\mu$s about the focal time[7].

The lack of exact agreement between the source and the retro-focal waveforms is due to the attenuation of the medium (small but not absent), to the effects related to the elastic wave propagation (mode conversion at the boundaries and single-mode transducers), to the nearby boundary reflections and to the TRM transducer ringdown. However, in both cases, the time symmetry about $t = 0\,\mu$s of the TR reconstructed source signal still holds, without significant dependence upon the TRM transducer size, though the experimental limitations depart from the ideal conditions under which the conservation of symmetry was theoretically proved in section 3. In addition, the quality of the reconstruction of the source signal is higher with the 3D laboratory specimen than with the 2D simulated one, as a consequence of increased wave front mixing going from 3D to 2D (see section 4.1).

6. Discussion and conclusions

In this paper, we investigate the roles of finite-size single-mode piezo-ceramic transducers bonded to the surface of a solid specimen in TR reconstruction of a temporally symmetric source. We intentionally choose to perform TR source reconstruction numerical simulations and laboratory

[7] Note that the amplitudes of the time series displayed in figures 11 and 12 are not significant relative to each other because different amounts of amplification were applied in each TR backpropagation to maximize signal-to-noise ratio.

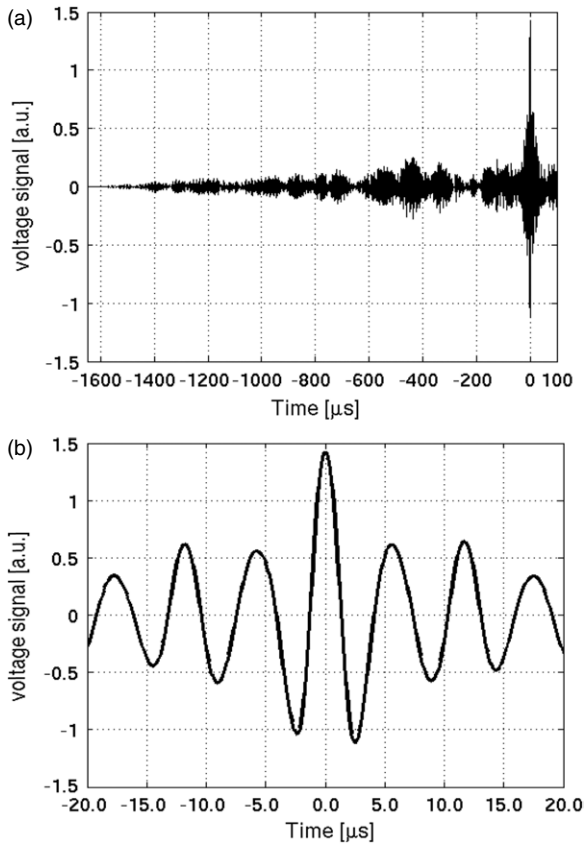

Figure 12. (*a*) Retro-focal signal at the forward propagation source location recorded during the TR backpropagation. The time axis has been shifted to 0. (*b*) Close-up around the retro-focal time. Experimental results for the case with the small TRM receiver.

experiments using a simple and limited configuration for a TRA experiment, i.e. using only one TRM transducer in a specimen that does not produce chaotic and ergodic wave front path dynamics. A sufficiently long TR window length guarantees retro-focusing with only one TR transducer due to the multiple reflections at the boundaries. We use this configuration because practical applications of TRA to NDE may have these limitations. For example, this type of single channel TRM setup has been used in an experiment for the location and characterization of a surface crack in a solid specimen, taking advantage of its nonlinear scattering behaviour for distinguishing it from another type of defect like an inhomogeneity [18].

Led by a theoretical analysis of a *gedanken* TRA experiment and by laboratory investigation in solids in general, we conduct the single element TRM source reconstruction simulation and experiment changing the size of the TRM transducer.

The results of both the numerical simulations and the laboratory experiments show that the retro-focusing process is robust despite using a single TRM transducer, based on the temporal symmetry around the focal time. There are significant differences between the two cases, as evidenced by the comparison between figures 9 and 10: with the large transducer the focus is less clear and energy is significantly redistributed about the sample during backpropagation. This result is due to the large diameter of the TRM transducer compared with the central wavelength. By extension, we infer that for transducer diameter greater than the central wavelength in general, energy redistribution in the backward propagation will be significant. However, spatial reciprocity is not violated.

Despite the loss of information, the TR process nonetheless conserves one important property of the source signal, its symmetry in time. The results suggest that one criterion for evaluating the quality and robustness of TRA experiments in solid media consists in calculating the level of symmetry around the retro-focal time, point by point, in a specimen.

Acknowledgments

This work was supported by Institutional Support (LDRD) at the Los Alamos National Laboratory. M Griffa acknowledges collaboration with the Bioinformatics and High Performance Computing Lab of the Bioindustry Park of Canavese, Colleretto Giacosa (Torino), Italy, the discussions with D Pasqualini and P P Delsanto and the help of M Scalerandi and A Gliozzi with the 2D LISA FDTD computational code.

Appendix A. Attenuation and the TRP in solid media

As cited in section 1, in the case of attenuative media the symmetry property of the wave equation is no longer valid. However, the TRP still holds but with decreased efficiency: part of the spatial frequencies associated with the forward propagating wave fields never reach the TRM due to dissipation. The backpropagated wave fields still retro-focus on the position(s) of the source(s) and/or point-like scatterer(s) from the forward propagation. The retro-focusing occurs also onto extended scatterers as long as they can be described as a collection of independent point-like scatterers. It takes place automatically since all the information about the positions of the sources is encoded in the signals themselves as recovered and recorded during the first stage [1].

From a signal processing point of view, this property is consistent with the demonstration of the TRP being a realization of the spatial-temporal matched filter to the set of the medium's Green functions from each TRM element to the original source/scatterer location [2, 6, 54, 62]. The basic principle of determining the matched filter for a linear system with a certain impulse response function consists of finding the right input signal in order to maximize the output of the system with respect to that response function. The demonstration only relies on the hypotheses of a linear elastic medium, the validity of the spatial reciprocity principle and the invariance in time of its properties. Thus, it is also valid for the TRP in attenuative media. However, a matched filter does not imply any constraint to the output signal off the matched location in space and time. That is where the attenuative properties of the medium strongly affect the retro-focusing process and therefore the reconstruction of the original source, changing the side lobes of the focusing profiles both in time and space.

Appendix B. Properties of convolution-in-time integrals

Appendix B.1. Property I

Given the definition of the signal created at the location $\boldsymbol{r}_B$ during the forward propagation by the source signal $s(t)$ at $\boldsymbol{r}_A$, $s_B(t) = \big(\tilde{G}_{B,A}(t') *_{t'} s(t')\big)(t)$

$$= \int_{-\infty}^{+\infty} \mathrm{d}t' \tilde{G}_{B,A}(t - t')s(t'), \tag{B.1}$$

its time-reversed version can be written as

$$s_B(-t) = \int_{-\infty}^{+\infty} \mathrm{d}t' \tilde{G}_{B,A}(-t - t')s(t'). \tag{B.2}$$

Making the change in time variable $t' = -t''$, equation (B.2) can be rewritten as

$$s_B(-t) = \int_{-\infty}^{+\infty} \mathrm{d}t'' \tilde{G}_{B,A}(-(t - t'')s(-t'')). \tag{B.3}$$

The expression on the right-hand side of equation (B.3) is equivalent to

$$s_B(-t) = \big(\tilde{G}_{B,A}(-t') *_{t'} s(-t')\big)(t). \tag{B.4}$$

Appendix B.2. Property II

The auto-correlation function of a signal represented by a real-valued function $f(t)$ can be expressed in terms of the convolution-in-time product of the function and its time-reversed version. Indeed, the auto-correlation function of $f(t)$ is defined as

$$AC[f](t) \equiv \int_{-\infty}^{+\infty} f(t')f(t' + t)\,\mathrm{d}t'. \tag{B.5}$$

Making the change in time variable $t'' = t' + t$ inside the integral in equation (B.5) leads to the following definition:

$$AC[f](t) = \int_{-\infty}^{+\infty} f(-(t - t'')f(t'')\,\mathrm{d}t''. \tag{B.6}$$

Equation (B.6) corresponds to

$$AC[f](t) = \big(f(t'') *_{t''} f(-t'')\big)(t). \tag{B.7}$$

Appendix B.3. Property III

The auto-correlation function of a signal $f(t)$ is an even function.

We calculate $AC[f](-t)$:

$$AC[f](-t) \equiv \int_{-\infty}^{+\infty} \mathrm{d}t' f(t')f(t' - t). \tag{B.8}$$

Then, we introduce in the integral of equation (B.8) the change in time variable $t'' = t - t'$ that leads to

$$AC[f](-t) = \int_{-\infty}^{+\infty} \mathrm{d}t'' f(t - t'')f(-t''). \tag{B.9}$$

Another change in temporal frame of reference, $t'' = -t'''$, leads to

$$AC[f](-t) = \int_{-\infty}^{+\infty} \mathrm{d}t''' f(t + t''')f(t''') = AC[f](t). \tag{B.10}$$

Appendix B.4. Property IV

Given two even functions $a(t)$ and $b(t)$ representing two signals symmetric about $t = 0$, their convolution-in-time is still an even function:

$$(a(t) *_t b(t))(-\tau) = \int_{-\infty}^{+\infty} \mathrm{d}t' a(-\tau - t')b(t'). \tag{B.11}$$

Considering that $a(-\tau - t') = a(\tau + t')$ and applying the change in variable $t' = -t''$ in the integral of equation (B.11):

$$(a(t) *_t b(t))(-\tau) = \int_{-\infty}^{+\infty} \mathrm{d}t'' a(\tau - t'')b(-t''). \tag{B.12}$$

Then, considering that $b(-t'') = b(t'')$, it results that

$$(a(t) *_t b(t))(-\tau) = \int_{-\infty}^{+\infty} \mathrm{d}t'' a(\tau - t'')b(t'')$$
$$= (a(t) *_t b(t))(\tau). \tag{B.13}$$

Appendix C. Calculations regarding finite-size TRM transducers

In the case where the source A of the forward propagation is point-like, located at $\boldsymbol{r}_A$, and B is a finite-size TR receiver covering a region (surface) R_B, the same procedure leading to equation (6) is valid and equation (6) can be simply rewritten as

$$s_A(t) = \frac{1}{V_{R_B}^2} \int_{R_B} \mathrm{d}\boldsymbol{r}_B \int_{R_B} \mathrm{d}\boldsymbol{r}'_B \big[(G(\boldsymbol{r}_A, \boldsymbol{r}_B, t')$$
$$*_{t'} G(\boldsymbol{r}_A, \boldsymbol{r}'_B, t')) *_{t'} s(-t')\big], \qquad \forall t \in [-t_R; t_R], \tag{C.1}$$

where $\tilde{G}(\boldsymbol{r}_A, \boldsymbol{r}_B, t - t')$ is the Green function for the medium evaluated at time t at the position $\boldsymbol{r}_A$ for a source at $\boldsymbol{r}_B$ emitting at time t', $\tilde{G}(\boldsymbol{r}_A, \boldsymbol{r}_B, t - t') = G(\boldsymbol{r}_A, \boldsymbol{r}_B, t, t')$, $\int_{R_B} \mathrm{d}\boldsymbol{r}_B$ indicates the integration over region R_B and V_{R_B} is the Euclidean measure of the manifold (surface area) R_B. Equation (C.1) is obtained from equation (6) applied to each point of R_B and using the principle of linear superposition. The same result from equation (6), i.e. the fact that $s_A(t)$ is symmetric about $t = 0$, is then valid in the case of the mean value over R_B of the wave field received on R_B and re-broadcast from it.

More generally, the symmetry property of $s_A(t)$ still holds also for the case of A having finite size covering a region R_A, the same type of procedure being used in order to calculate the mean value of the emitted and received wave field from/on R_A.

References

[1] Fink M, Prada C, Wu F and Cassereau D 1989 Self focusing with time reversal mirror in inhomogeneous media *Proc. IEEE Ultrasonics Symp. 1989 (Montreal, PQ, Canada)* (Piscataway, NJ: IEEE) pp 681–6

[2] Fink M, Cassereau D, Derode A, Prada C, Roux P, Tanter M, Thomas J L and Wu F 2000 Time-reversed acoustics *Rep. Prog. Phys.* **63** 1933–95

[3] Wu F, Thomas J L and Fink M 1992 Time reversal of ultrasonic fields: II. Experimental results *IEEE Trans. Ultrason. Ferroelectr. Freq. Control* **39** 567–78

[4] Fink M and Prada C 2001 Acoustic time-reversal mirrors *Inverse Problems* **17** R1–R38

[5] Fink M 1992 Time reversal of ultrasonic fields: I. Basic principles *IEEE Trans. Ultrason. Ferroelectr. Freq. Control* **39** 555–66

[6] Cassereau D and Fink M 1992 Time-reversal of ultrasonic fields: III. Theory of the closed time-reversal cavity *IEEE Trans. Ultrason. Ferroelectr. Freq. Control* **39** 579–92

[7] Cassereau D and Fink M 1993 Focusing with plane time-reversal mirrors: an efficient alternative to closed cavities *J. Acoust. Soc. Am.* **94** 2373–86

[8] Fink M 1997 Time reversed acoustics *Phys. Today* **50** (3) 34–40

[9] Anderson B E, Griffa M, Larmat C, Ulrich T J and Johnson P A 2008 Time reversal *Acoust. Today* **4** (1) 5–16

[10] Kupperman W A, Hodgkiss W S, Song H, Akal T, Ferla C and Jakson D 1998 Phase conjugation in the ocean: experimental demonstration of an acoutical time reversal mirror *J. Acoust. Soc. Am.* **103** 25–40

[11] Draeger C and Fink M 1997 One-channel time reversal of elastic waves in a chaotic 2d-silicon cavity *Phys. Rev. Lett.* **79** 407–10

[12] Draeger C and Fink M 1999 One-channel time-reversal in chaotic cavities: theoretical limits *J. Acoust. Soc. Am.* **105** 611–7

[13] Draeger C and Fink M 1999 One-channel time-reversal in chaotic cavities: experimental results *J. Acoust. Soc. Am.* **105** 618–25

[14] de Rosny J and Fink M 2002 Overcoming the diffraction limit in wave physics using a time-reversal mirror and a novel acoustic sink *Phys. Rev. Lett.* **89** 124301

[15] Sutin A, TenCate J A and Johnson P A 2004 Single-channel time reversal in elastic solids *J. Acoust. Soc. Am.* **116** 2779–84

[16] Montaldo G, Palacio D, Tanter M and Fink M 2004 Time reversal kaleidoscope: a smart transducer for three-dimensional ultrasonic imaging *Appl. Phys. Lett.* **84** 3879–81

[17] Prada C, Kerbrat E, Cassereau D and Fink M 2002 Time reversal techniques in ultrasonic nondestructive testing of scatering media *Inverse Problems* **18** 1761–73

[18] Ulrich T J, Johnson P A and Sutin A 2006 Imaging nonlinear scatterers applying the time reversal mirror *J. Acoust. Soc. Am.* **119** 1514–8

[19] Guyer R A and Johnson P A 1999 Nonlinear mesoscopic elasticity: Evidence for a new class of materials *Phys. Today* **52** (4) 30–6

[20] Johnson P A 1999 The new wave in acoustic testing *Mater. World, J. Inst. Mater.* **7** 544–6

[21] Johnson P A 2006 *Nonequilibrium Nonlinear Dynamics in Solids: State of the Art* (Berlin: Springer) pp 49–69 chapter 4

[22] Gliozzi A S, Griffa M and Scalerandi M 2006 Efficiency of time-reversed acoustics for nonlinear damage detection in solids *J. Acoust. Soc. Am.* **120** 2506–17

[23] Ulrich T J, Johnson P A and Guyer R A 2007 Interaction dynamics of elastic waves with a complex nonlinear scatterer through the use of a time reversal mirror *Phys. Rev. Lett.* **98** 104301

[24] Goursolle T, Callé S, Dos Santos S and Bou Matar O 2007 A two-dimensional pseudospectral model for time reversal and nonlinear elastic wave spectroscopy *J. Acoust. Soc. Am.* **122** 3220–9

[25] Macovski A 1979 Ultrasound imaging using arrays *Proc. IEEE* **67** 484–96

[26] Kummer W H 1992 Basic array theory *Proc. IEEE* **80** 127–40

[27] Parker D and Zimmerman D C 2002 Phased arrays: I. Theory and architectures *IEEE Trans. Microw. Theory Tech.* **50** 678–87

[28] Ylitalo J T and Emert H 1994 Ultrasound synthetic aperture imaging: Monostatic approach *IEEE Trans. Ultrason. Ferroelectr. Freq. Control* **41** 333–9

[29] Jensen J A, Nikolov S I, Gammelmark K L and Pedersen M H 2006 Synthetic aperture ultrasound imaging *Ultrasonics* **44** e5–e15

[30] Wang C H, Rose J T and Chang F-K 2003 A computerized time-reversal method for structural health monitoring *Proc. SPIE* **5046** 4858–69

[31] Chun H W, Rose J T and Chang F-K 2004 A synthetic time-reversal imaging method for structural health monitoring *Smart Mater. Struct.* **13** 415–23

[32] Fink M, Montaldo G and Tanter M 2003 Time reversal acoustics in biomedical engineering *Annu. Rev. Biomed. Eng.* **5** 465–97

[33] Robert J-L, Burcher M, Cohen-Bacrie C and Fink M 2006 Time reversal operator decomposition with focused transmission and robustness to speckle noise: application to microcalcification detection *J. Acoust. Soc. Am.* **119** 3848–59

[34] Thomas J-L, Wu F and Fink M 1996 Time reversal focusing applied to lithotripsy *Ultrason. Imag.* **18** 106–21

[35] Thomas J-L and Fink M 1996 Ultrasonic beam focusing through tissue inhomogeneities with a time reversal mirror: application to transskull therapy *IEEE Trans. Ultrason. Ferroelectr. Freq. Control* **43** 1122–9

[36] Tanter M, Thomas J-L and Fink M 1998 Focusing and steering through absorbing and aberrating layers: application to ultrasonic propagation through the skull *J. Acoust. Soc. Am.* **103** 2403–10

[37] Spies M and Jager W 2003 Synthetic aperture focusing for defect reconstruction in anisotropic media *Ultrasonics* **41** 125–31

[38] Hannemann R 2001 Modeling and imaging of elastodynamic wave fields in inhomogeneous anisotropic media *PhD Thesis* University of Kassel

[39] Lingvall F, Wu P and Stepinski T 2003 Inspection of copper canisters for spent nuclear fuel by means of ultrasound. nonlinear acoustics, synthetic aperture imaging *SKB Technical Report* TR-03-05, Signals and Systems Division, Department of Materials Science, Uppsala University

[40] Shlivinski A and Langerberg K J 2007 Defect imaging with elastic waves in inhomogeneous-anisotropic materials with composite geometries *Ultrasonics* **46** 89–104

[41] Derode A, Roux P and Fink M 1995 Robust acoustic time reversal with high order multiple scattering *Phys. Rev. Lett.* **75** 4206–9

[42] Roux P, Roman B and Fink M 1997 Time-reversal in an ultrasonic waveguide *Appl. Phys. Lett.* **70** 1811–3

[43] Tanter M, Thomas J-L and Fink M 1998 Influence of boundary conditions on time-reversal focusing through heterogeneous media *Appl. Phys. Lett.* **72** 2511–3

[44] Montaldo G, Perez N, Negreira C and Fink M 2007 The spatial focusing of a leaky time reversal chaotic cavity *Waves Random Complex Media* **17** 67–83

[45] Roux P and Fink M 2000 Time-reversal in a waveguide: Study of the temporal and spatial focusing *J. Acoust. Soc. Am.* **107** 2418–29

[46] Kupermann W A and Jackson D R 2002 Ocean acoustics matched-field processing and phase conjugation *Imaging of Complex Media with Acoustic and Seismic Waves (Topics in Applied Physics vol 84)* (Berlin: Springer) pp 43–97

[47] Kupermann W A, Hodgkiss W S, Song H C, Akal T, Ferla C and Jackson D 1998 Phase conjugation in the ocean: experimental demonstration of an acoustic time-reversal mirror *J. Acoust. Soc. Am.* **103** 25–40

[48] Kim S, Edelmann G F, Kupermann W A, Hodgkiss W S, Song H C and Akal T 2001 Spatial resolution of time-reversal arrays in shallow water *J. Acoust. Soc. Am.* **110** 820–9
[49] Lingevitch J F, Song H C and Kupermann W A 2002 Time reversed reverberation focusing in a waveguide *J. Acoust. Soc. Am.* **111** 2609–14
[50] Kim S, Kupermann W A, Hodgkiss W S, Song H C, Edelmann G F and Akal T 2003 Robust time reversal focusing in the ocean *J. Acoust. Soc. Am.* **114** 145–57
[51] Ing R K and Fink M 1998 Time-reversed lamb waves *IEEE Trans. Ultrason. Ferroelectr. Freq. Control* **45** 1032–43
[52] Wells P N T 1999 Ultrasonic imaging of the human body *Rep. Prog. Phys.* **62** 671–722
[53] Derode A, Tourin A and Fink M 2000 Limits of time-reversal focusing through multiple scattering: long-range correlation *J. Acoust. Soc. Am.* **107** 2987–98
[54] Tanter M, Thomas J-L and Fink M 2000 Time reversal and the inverse filter *J. Acoust. Soc. Am.* **108** 223–34
[55] Nunez I and Negreira C 2005 Efficiency parameters in time reversal acoustics: applications to dispersive media and multimode wave propagation *J. Acoust. Soc. Am.* **117** 1202–9
[56] Tournat V, Profunser D M, Muramoto E, Matsuda O, Takezaki T, sueoka S and Wright O B 2006 Microscale multiple scattering of coherent surface acoustic wave packets probed with gigahertz time-reversal acoustics *Phys. Rev.* E **74** 026604
[57] Draeger C, Cassereau D and Fink M 1997 Theory of the time-reversal process in solids *J. Acoust. Soc. Am.* **102** 1289–95
[58] Delsanto P P, Johnson P A, Scalerandi M and TenCate J A 2002 Lisa simulations of time-reversed acoustic and elastic wave experiments *J. Phys. D: Appl. Phys.* **35** 3145–52
[59] Aki K and Richards P G 1980 *Quantitative Seismology* vol I, 1st edn (San Francisco: Freeman) pp 64–77 chapter 4
[60] Aki K and Richards P G 1980 *Quantitative Seismology* vol I, 1st edn (San Francisco, CA: Freeman)
[61] Barton G 1989 *Elements of Green's Functions and Propagation. Potentials, Diffusion and Waves* (Oxford: Oxford University Press)
[62] Dorme C and Fink M 1995 Focusing in transmit-receive mode through inhomogeneous media: the time reversal matched filter approach *J. Acoust. Soc. Am.* **98** 1155–62
[63] Cassereau D and Fink M 1993 Focusing with plane time-reversal mirrors: an efficient alternative to closed cavities *J. Acoust. Soc. Am.* **94** 2373–86
[64] Stepanishen P R 1971 Transient radiation from pistons in an infinite planar baffle *J. Acoust. Soc. Am.* **49** 1629–38
[65] Harris G H 1981 Review of transient field theory for a baffled planar piston *J. Acoust. Soc. Am.* **70** 10–20
[66] Harris G R 1981 Transient field of a baffled planar piston having an arbitrary vibration amplitude distribution *J. Acoust. Soc. Am.* **70** 186–204
[67] Cassereau D, Guyomar D and Fink M 1988 Time deconvolution of diffraction effects-application to calibration and prediction of transducer waveforms *J. Acoust. Soc. Am.* **84** 1073–85
[68] Stansfield D 1991 *Underwater Electroacoustic Transducers*, (Los Altos Hills, CA: Peninsula Publishing) chapter 6
[69] Blake W K and Chase D M 1971 Wavenumber-frequency spectra of turbulent-boundary-layer pressure measured by microphone arrays *J. Acoust. Soc. Am.* **49** 862–77
[70] Delsanto P P, Whitcombe T, Chaskelis H H and Mignogna R B 1992 Connection machine simulation of ultrasonic wave propagation in materials: I. The one-dimensional case *Wave Motion* **16** 65–80
[71] Delsanto P P, Schechter R S, Chaskelis R S, Mignogna R B and Kline R 1994 Connection machine simulation of ultrasonic wave propagation in materials: I. The two-dimensional case *Wave Motion* **20** 295–314
[72] 1997 Connection machine simulation of ultrasonic wave propagation in materials: I. The three-dimensional case *Wave Motion* **26** 329–39
[73] Schechter R S, Chaskelis H H, Mignogna R B and Delsanto P P 1994 Real-time parallel computation and visualization of ultrasonic pulses in solids *Science* **265** 1188–92
[74] Courant R, Friedrichs K and Lewy H 1967 On the partial difference equations of mathematical physics *IBM J.* 215–34 (Republished version)
[75] Delsanto P P, Iordache D, Iordache C and Ruffino E 1997 Analysis of stability and convergence in fd simulations of the 1-d ultrasonic wave propagation *Math. Comput. Modelling* **25** 19–29
[76] Iordache D, Delsanto P P and Scalerandi M 1997 Pulse distortions in the fd simulation of elastic wave propagation *Math. Comput. Modelling* **25** 31–43